A Study on Exposure to Electromagnetic Fields From User Equipment Antennas above 100 GHz

Yao, Ming; Zhekov, Stanislav Stefanov; Xu, Bo; Li, Kun; Zhang, Shuai

Published in:
I E E E Transactions on Electromagnetic Compatibility

DOI (link to publication from Publisher):
10.1109/TEMC.2023.3262322

Publication date:
2023

Document Version
Accepted author manuscript, peer reviewed version

A Study on Exposure to Electromagnetic Fields From User Equipment Antennas above 100 GHz

Ming Yao, *Student Member, IEEE,* Stanislav Stefanov Zhekov, Bo Xu, *Member, IEEE,* Kun Li, *Member, IEEE,* and Shuai Zhang, *Senior Member, IEEE*

***Abstract*—The next-generation mobile communication technology may exploit the higher frequency spectrum beyond 100 GHz, while most studies on electromagnetic field (EMF) exposure from mobile communication devices focus on frequencies below 100 GHz. In this paper, the EMF exposure from sub-terahertz antennas designed for future mobile communication is evaluated with a multilayer flat tissue phantom. It is demonstrated that the deposited EMFs can be evaluated by neglecting the deep tissue in the simplified phantom. Then, the temperature distribution in the full-size phantom can be evaluated using the solution to the simplified electromagnetic problem to reduce the overall computation time. Considering different sizes of the averaging area for absorbed power density, the results show a good correlation between the peak absorbed power density averaged over a small area of around one square centimeter and the peak rising temperature.**

***Index Terms*—EMF exposure, 6G, sub-THz spectrum, user equipment, absorbed power density.**

I. Introduction

THE next-generation (6G) mobile communication networks are expected to be launched in the 2030s. The sub-terahertz (THz) and THz spectrum beyond 100 GHz are under consideration for 6G. Above 100 GHz, there are opportunities for relatively large amounts of spectrum, but, given the very challenging propagation conditions, it is mainly of interest for very specific scenarios requiring extreme traffic capacity and/or data rates in a dense network deployment condition [1]. Like the previous generations, wireless 6G devices and equipment need to comply with the relevant electromagnetic field (EMF) exposure limits.

The most widely adopted EMF exposure limits are provided in the guidelines established by the International Commission on Non-Ionizing Radiation Protection (ICNIRP), and the ICNIRP guidelines covering the range 100 kHz to 300 GHz were recently updated in 2020 [2]. Basic restrictions are derived with large safety margins to prevent whole-body and localized tissue heating [2]. Below 6 GHz, the basic restrictions for local exposure averaged over 6 minutes are set in terms of specific absorption rate (SAR), which is averaged over 10 g of tissue. Above 6 GHz, the counterpart is absorbed power density (APD). According to [2], APD should be averaged over 4 cm^2 from 6 to 300 GHz and also over 1 cm^2 for frequencies ranging from 30 to 300 GHz. Most relevant APD studies focus on the frequency range below 100 GHz, e.g., [3]–[7]. Some studies only utilize plane wave sources [8], [9], single-layer phantoms [10], or one-dimensional analytical analysis [11]. Therefore, there is a need for further investigations of EMF exposure from realistic antennas covering the frequency over 100 GHz, which may be used for future 6G communication.

As basic restrictions might be difficult to evaluate, reference levels are specified by [2] using a more practical set of quantities derived from the basic restrictions. Above 6 GHz, the reference levels are set in terms of incident power density (IPD), but it cannot be used to determine compliance in the reactive near field according to [2]. There have been a few works addressing the IPD evaluation for millimeter-wave devices e.g., [12]–[14]. Nevertheless, this paper focuses on the APD for the target frequency range.

In this paper, cavity patch antenna array designs at 100, 150, and 200 GHz as the mobile user equipment are used, which might be used for 6G communication because of its small volume, low profile, wide beamwidth, and broad bandwidth. The APD, tissue temperature elevation, and the heating factor (HF) are assessed, as well as their correlations with the averaging area of APD, the array size, and the frequency.

II. Model, Dosimetry, and Method

A. Exposure Scenarios

In this study, 2 × 2, 4 × 4, and 6 × 6 planar cavity patch arrays at 100, 150, and 200 GHz with high gain and broad bandwidth are designed and assumed for 6G applications. The antenna arrays are loaded with a substrate of Rogers 4350B laminate (relative permittivity of 3.66 and loss tangent of 0.0037). For each array, the inter-element spacing is 0.5λ where λ is the free-space wavelength. The configuration of the 6 × 6 antenna array at 100 GHz is shown in Fig. 1. The 2 × 2 and 4 × 4 arrays use the same element design and inter-element spacing.

The antenna arrays are placed at a distance, d, away from a 4-layer flat phantom based on the tissue thicknesses of the forearm model [9], as shown in Fig. 2. In this study, the range of d was set to be $1-9$ mm, which transitions from the reactive

This work done by Ming Yao was supported in part by the China Scholarship Council.

Ming Yao, Stanislav Stefanov Zhekov, and Shuai Zhang are with the Propagation and Millimeter-Wave Systems Section, Department of Electronic Systems, Aalborg University, 9220 Aalborg, Denmark (e-mail: sz@es.aau.dk).

Stanislav Stefanov Zhekov is also with Ericsson Research, Ericsson AB, 16480 Stockholm, Sweden.

Bo Xu is with Ericsson Research, Ericsson AB, 16480 Stockholm, Sweden.

Kun Li is with the Faculty of Engineering and Design, Kagawa University, Takamatsu 761-0396, Japan.

near field to the radiated near field. The permittivity and conductivity of the tissue of this phantom are extracted from [9, Fig. 4]. Other parameters of the phantom are provided in Table I. The total input power of the arrays is set to 12 dBm.

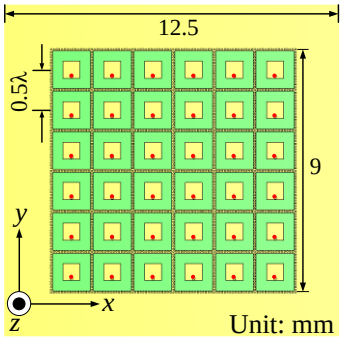

Fig. 1. Illustration of studied 6 × 6 antenna array at 100 GHz, where red dots are feeding points.

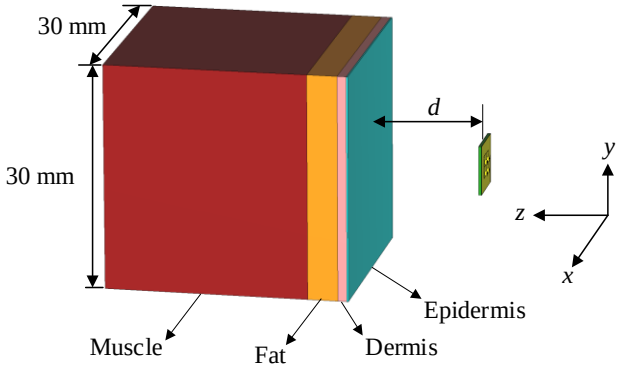

Fig. 2. The exposure scenario with a 4-layer forearm phantom.

TABLE I
SOME PARAMETERS OF THE 4-LAYER FOREARM PHANTOM

	Epidermis	Dermis	Fat	Muscle
K (W/(m^2·°C))	0.42	0.42	0.25	0.5
B (W/(m^3·°C))	0	9100	1700	2700
ρ (kg/m^3)	1109	1109	911	1090
Thickness of full-size phantom (mm)	0.2	1.2	4	27
Thickness of simplified phantom (mm)	0.2	1.2	1	

B. Dosimetry Analysis

The temperature in tissue associated with EMFs can be evaluated by Pennes's bioheat transfer equation (BHTE) [15]. The steady-state form is

$$\nabla \cdot \big(K(\boldsymbol{r})\nabla T(\boldsymbol{r})\big) + \rho(\boldsymbol{r})SAR(\boldsymbol{r}) - B(\boldsymbol{r})\big(T(\boldsymbol{r}) - T_{\mathrm{B}}(\boldsymbol{r})\big) = 0, \quad (1)$$

where T and K represent the temperature and thermal conductivity of the tissue, respectively, B and T_{B} denote perfusion and temperature of the blood, respectively, and $\boldsymbol{r}$ is the position coordinate. Eq. (1) is denoted as the thermal problem in this paper. SAR is defined by [2]

$$SAR(\boldsymbol{r}) = \frac{\sigma(\boldsymbol{r})}{2\rho(\boldsymbol{r})}|\boldsymbol{E}(\boldsymbol{r})|^2, \quad (2)$$

where $\boldsymbol{E}$ denotes the complex electric field, and σ and ρ are the electrical conductivity and mass density of the tissue, respectively. The BHTE is one of several theoretical models that have been proposed for heat transfer in vascularized tissues, all of which are approximations [16] –[21]. The validity of the BHTE is discussed well in [16].

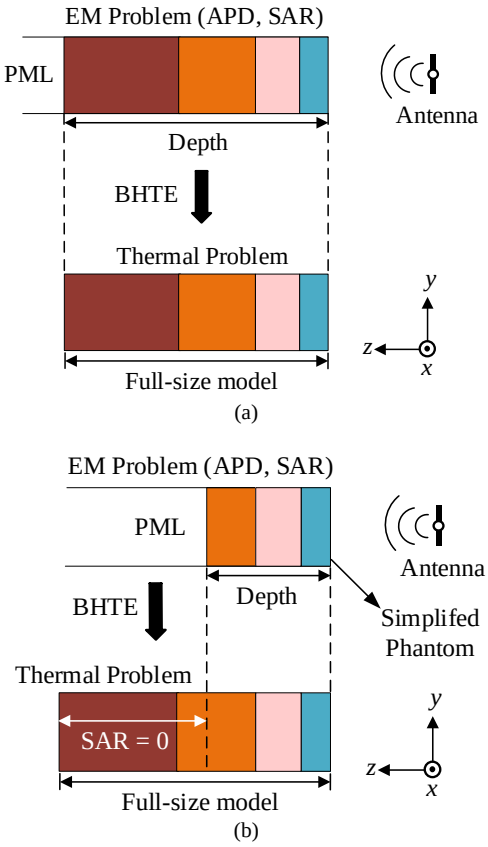

Fig. 3. Schematic view of dosimetry approaches (a) traditional assessment, where the phantom in the EM problem is the same as one in the thermal problem. (b) simplified assessment proposed in this study, where the thickness-reduced phantom was used in the EM problem and the full-size model in the thermal problem. The SAR, which is not computed in the EM problem in the deeper tissue, is enforced to be 0.

The peak temperature elevation ΔT is the maximum difference between the temperatures with and without considering EMF exposure. The spatially averaged APD, S_{ab}, is defined as [2]

$$S_{\mathrm{ab}} = \frac{1}{A}\iint_A dxdy \int_0^{z_{\max}} SAR(\boldsymbol{r})\,\rho(\boldsymbol{r})dz, \quad (3)$$

where the phantom surface is at $z = 0$, $z_{\max}$ is the depth of the phantom model, and A is the averaging area. Eqs. (2) and (3) are denoted as the electromagnetic (EM) problem. The boundary conditions for the EM problem and the thermal problem are set like in [22]. The full-wave simulation software CST Studio 2021 was used to solve both the EM and thermal problems. To evaluate the correlation between APD and ΔT,

HF is commonly used, which is defined as the ratio of ΔT to the peak APD averaged over a certain size of an area

$$HF(A) = \frac{\max \Delta T}{\max S_{\text{ab}}} \tag{4}$$

where S_{ab} is dependent on A.

C. Phantom Simplification

Traditionally, the phantom used in the EM problem is the same as the one in the thermal problem, as shown in Fig. 3(a). Due to the small penetration depth in the frequency range considered here, the thickness of the human tissue can be reduced for SAR and APD calculations to improve computation efficiency, as shown in Fig. 3(b). Then, the SAR distribution computed in the reduced phantom is imported into the thermal problem with the full-size phantom. As shown in Fig. 3(b), in the thermal problem, the SAR in the deeper tissue, which is not computed in the EM problem, is enforced to be 0. However, the phantom size in the thermal problem cannot be reduced, as the thermal problem is sensitive to the tissue thickness and boundary conditions.

TABLE II
COMPARISONS OF PEAK TEMPERATURE ELEVATION AND HF FOR DIFFERENT DEPTHS USED IN SIMPLIFIED EM PROBLEM

Reduced Depth		0.6	1	2.4	32.4 (Full-Model)
2 × 2 Array d = 1 mm at 100 GHz	ΔT (°C)	0.98	0.99	1.00	1.00
	HF (°Cm^2/W)	0.0016	0.0016	0.0019	0.0019
Plane-wave (Simulated)	ΔT (°C)	1.00	1.00	1.00	1.00
	HF (°Cm^2/W)	0.0193	0.0193	0.0233	0.0233
Plane-wave (Analytical)	ΔT (°C)	0.97	0.99	1.00	1.00
	HF (°Cm^2/W)	0.0223	0.0224	0.0208	0.0208

To validate such an approach and investigate the threshold of the minimum tissue depth used in the simplified EM problem, the APD and ΔT are assessed with different tissue depths in two scenarios. The first scenario uses the 2 × 2 array at 100 GHz with d = 1 mm, and the second scenario uses plane-wave illumination with normal incidence. For each scenario, the simplified method is compared to the traditional method by simulation. In addition, the one-dimensional analytical results for plane wave illumination with a varying-thickness phantom are also computed according to [8, Eqs. (1) – (2)], [9, Eqs. (3) – (7)]. For comparison, ΔT with the full-size model for both EM and thermal problems was set as the reference, named ΔT_{ref}. For the 2 × 2 array and plane wave illumination with different considered tissue depths in the EM problem, the total input power was adjusted such that $\Delta T_{\text{ref}} = 1$℃ in this subsection.

In Table II, it can be seen that the 2.4-mm depth in the simplified EM problem can reach very good accuracy of dosimetry assessment for both realistic antenna and plane wave evaluations over 100 GHz. Further reducing the tissue depth used in the simplified EM problem can still achieve good accuracy for thermal computation. The simplified method is applied to both the realistic antenna and plane-wave scenarios at 100 GHz in Table II. For other sub-THz frequencies above 100 GHz, the simplified phantom in the EM problem can be thinner because of the smaller penetration depth at higher frequencies. In this study, the results in section III are based on the 2.4 mm-simplified phantom (see Table I) for the EM problem and the full-size phantom for the thermal problem.

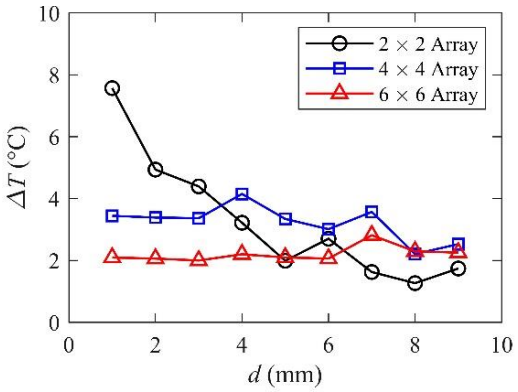

Fig. 4 Peak ΔT versus d for different array sizes at 100 GHz.

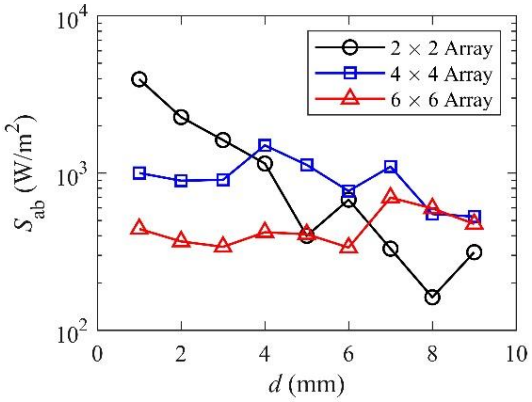

Fig. 5 Peak S_{ab} versus d for different array sizes at 100 GHz.

III. RESULTS AND DISCUSSION

The examples of the resulting temperature distributions in the phantom are shown in Appendix A. Fig. 4 shows the peak ΔT versus d for different array sizes at 100 GHz. From Appendix A and Fig. 4, it can be seen that the 2 × 2 array has larger ΔT at close distances, e.g., $d \leq 5$ mm. As d increases, the peak ΔT of the 2 × 2 array is lower compared to the larger arrays. Some oscillations for peak ΔT and APD can be observed about every half wavelength, which is line with the observations in the literature, e.g., [22], due to the standing waves between the antenna and phantom.

Fig. 6 shows that the statistical HF distributions vary with A and the array size at each frequency. Each bar, including a box and whisker, shows the mean value (the red line in the boxes), 25th and 75th percentiles (the bottom and top edges of the boxes), the minimum and maximum values (the bottom and top edges of whiskers) of HFs considering all studied d. It can be seen from Fig. 6 that a larger A leads to an increased HF at a fixed frequency and with given array size. A larger spread of HF distributions for A = 0 cm^2, i.e., peak APD, can be observed,

suggesting a poorer correlation. Fig. 7 shows the mean value μ_{HF} and 95% confidence interval of HFs for each choice of A by aggregating the HF results for all d, frequencies, and array sizes. It can be seen from Figs. 6 and 7 that the HF distributions of A = 0.75 and 1 cm^2 are closer to the HF corresponding to the plane wave scenario (see the dashed lines in Figs. 6 and 7). It means that when A is chosen around 1 cm^2, the HF is similar for both near-field and far-field exposure scenarios.

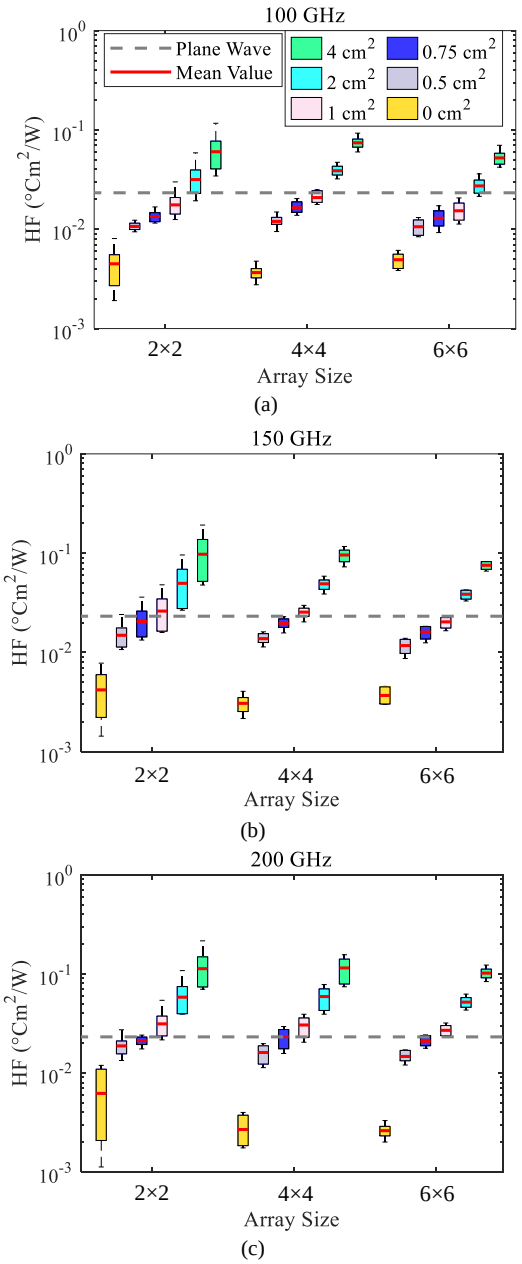

Fig. 6. HFs, in the logarithmic scale vary with array size at (a) 100 GHz; (b) 150 GHz; (c) 200 GHz. Each bar shows the 25th and 75th percentiles (bottom and top edges of box), the minimum and maximum values (bottom and top edges of whiskers) of HFs considering all the studied distances. The dashed lines indicate the HF of the plane-wave scenario with normal incidence.

Table III presents the coefficient of variation (CV) of HF for each A considering all d, frequencies, and array sizes. The CV is the ratio of the standard deviation σ_{HF} to the mean value μ_{HF} and is calculated for different sizes of A:

$$CV(A) = \frac{\sigma_{HF}(A)}{\mu_{HF}(A)}. \quad (5)$$

A smaller CV indicates a smaller deviation around the mean value. In Table III, CV = 49.8% for A = 0 cm^2, which is the largest among all studied A. In contrast, CV = 28% for A = 0.5 cm^2, which is the lowest among all A, then steadily increasing when A becomes larger. A moderate variation of HF for A around 1 cm^2 can be observed. Considering the results shown in Figs. 6 and 7 and in Table III, A around 1 cm^2 seems a good choice on balance, which is in line with the 1 cm^2 spatial averaging requirements in the ICNIRP guidelines above 30 GHz. Also, note that the results presented in this paper use fixed tissue thicknesses. The statistical study in [9] indicates that the HF is little affected by the dielectric properties but largely dependent on the tissue thickness. Future works might be needed to examine the effects of different tissue thicknesses on HFs and the choice of A above 100 GHz.

In [11], it is suggested that the peak APD (with A = 0 cm^2) might be used for EMF compliance assessments because it provides an additional safety factor compared with A = 1 and 4 cm^2, however, without considering the degrees of correlation. It should also be noted that the selected d is small corresponding to very localized exposure scenarios. When d increases, it is expected that HFs for A = 1 and 4 cm^2 will converge.

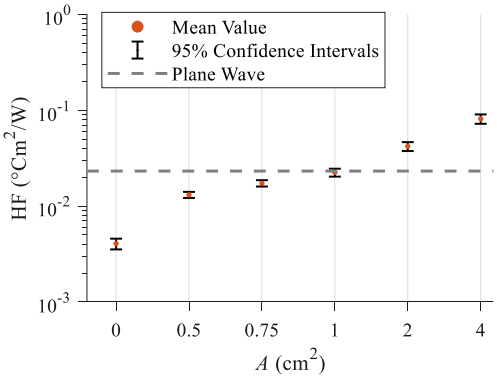

Fig. 7. HFs considering all d, frequencies, and array sizes for mean value and 95% confidence interval (in the logarithmic scale). The dashed lines indicate the HF of the plane-wave scenario with normal incidence.

TABLE III
CVs OF HF CONSIDERING ALL DISTANCES, FREQUENCIES, AND ARRAY SIZES FOR DIFFERENT AVERAGING AREA

A (cm^2)	0	0.5	0.75	1	2	4
CV (%)	49.8	28.0	29.5	36.7	41.2	43.5

V. Conclusion

In this study, we have investigated the correlation between APD for different averaging areas and temperature elevation in tissue using realistic antenna designs in the sub-THz spectrum. A simplified method has been proposed to reduce computational time, and it has been demonstrated that the simplified approach provides good accuracy in dosimetry computation. It has been observed that the HF increases with the array size, the frequency, and the size of the APD averaging area. The results suggest that a better correlation between temperature elevation and APD can be established over 100 GHz when APD is averaged over an area of around 1 cm^2 compared to using spatial peak APD values for realistic antennas placed at very close distances shorter than 10 mm. The findings are in line with the spatial averaging requirements specified in the international EMF exposure guidelines.

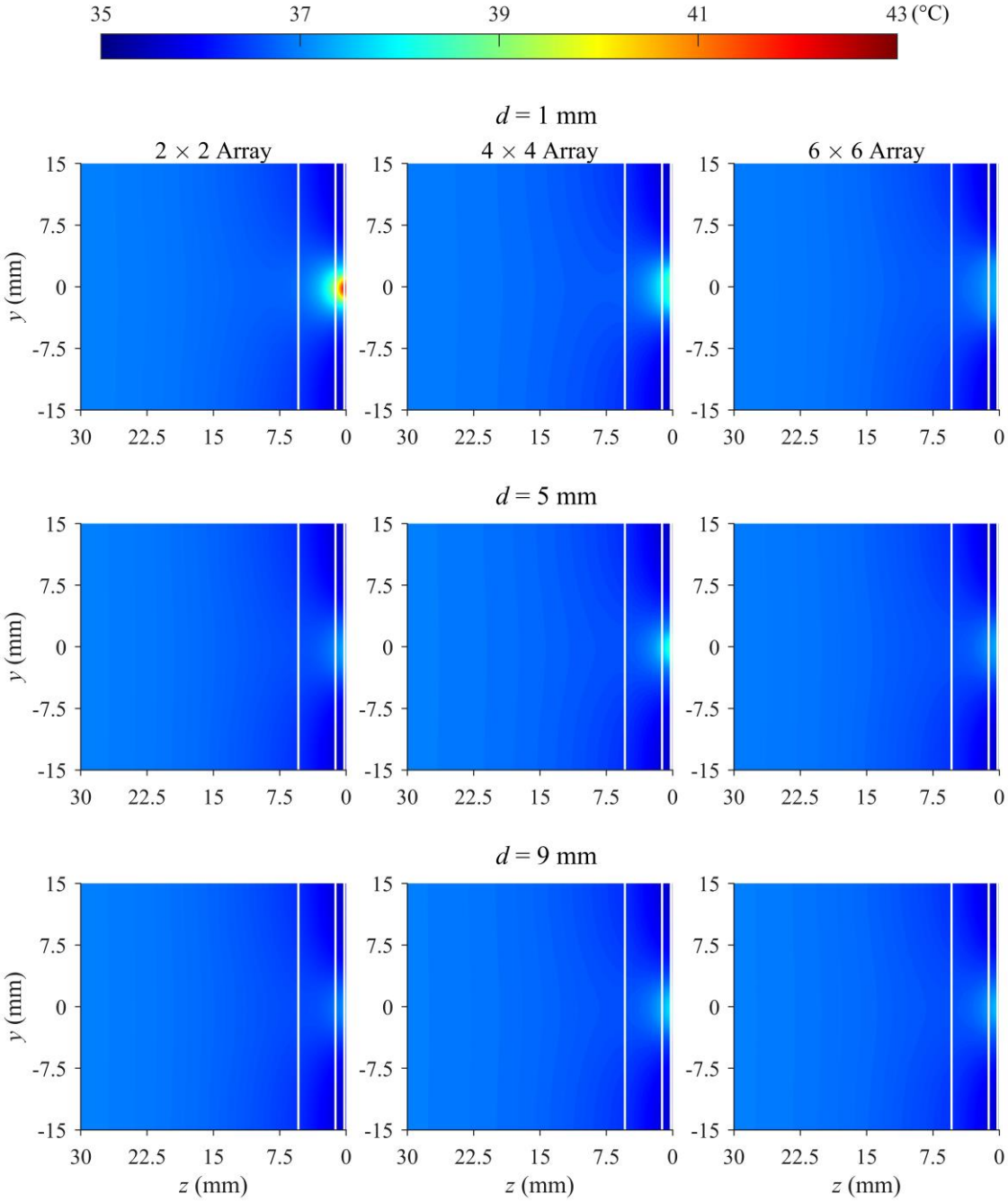

Fig. 8 Temperature distributions on the *yoz*-plane for different *d* (1, 5, 9 mm) and array sizes (2 × 2, 4 × 4, 6 × 6) at 100 GHz. The white lines are the interface between the different layers of the tissue models.

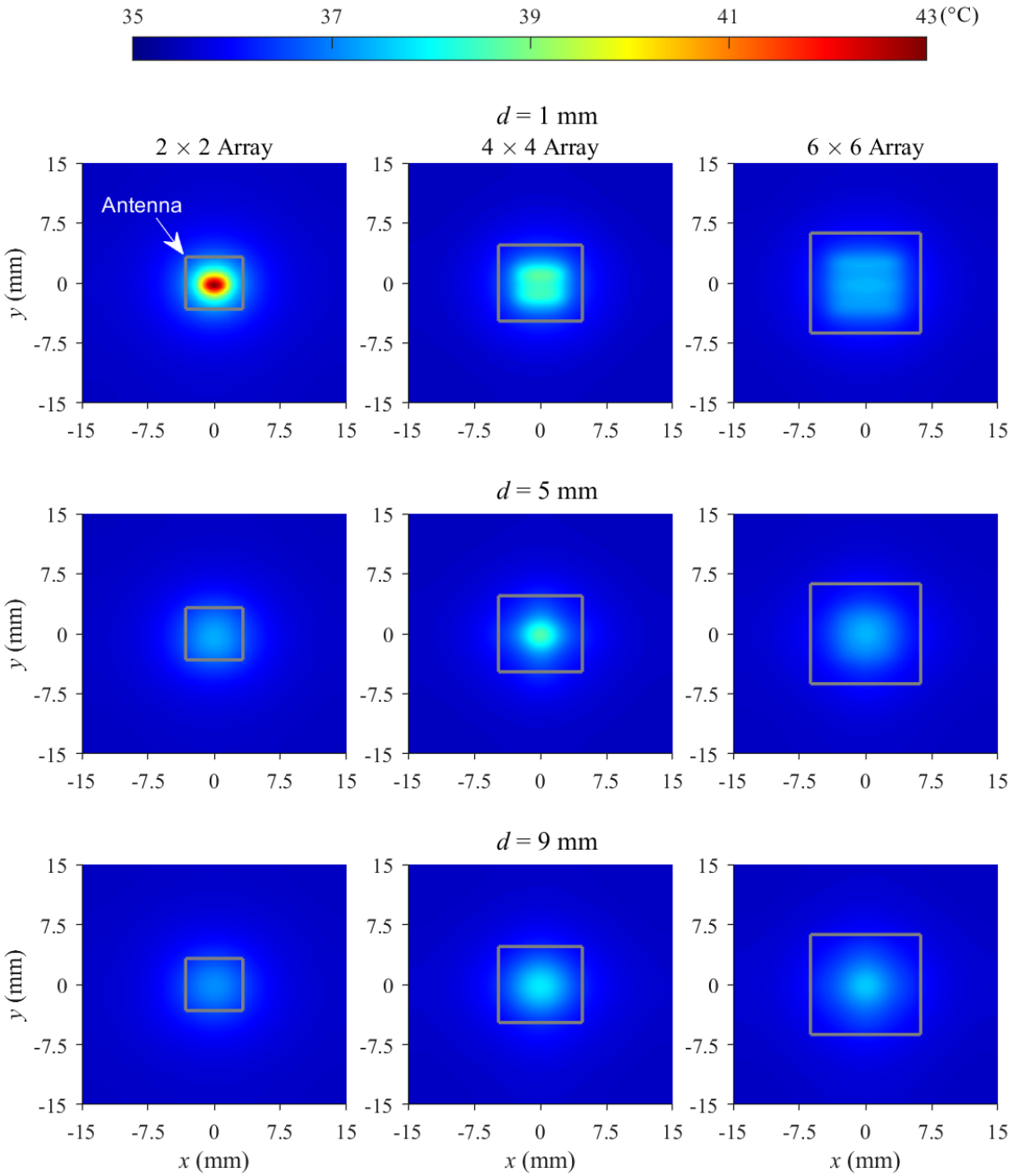

Fig. 9 Temperature distributions on the *xoy*- plane for different *d* (1, 5, 9 mm) and array sizes (2 × 2, 4 × 4, 6 × 6) at 100 GHz. The gray rectangle in each figure represents the antenna models.

APPENDIX A

Figs. 8 – 9 show the temperature distributions on the tissue phantom for different array sizes and distances. The coordinate system is shown in Fig. 1. The gray rectangles in Fig. 9 represent the antenna models. As mentioned in Section III, for the same input power, the larger temperature elevation for 2 × 2 array can be observed, and it is lower compared to other array sizes as *d* increases.

APPENDIX B

Figs. 10(a) and (b) show the SAR (on the *yoz*-plane) and APD derived from SAR distributions on the tissue phantom for different array sizes and distances, respectively. Similar to temperature distributions, for the same input power, the smaller array size provides more focused APD distribution at close distance.

ACKNOWLEDGEMENTS

The authors thank Christer Törnevik and Davide Colombi at Ericsson Research for their comments.

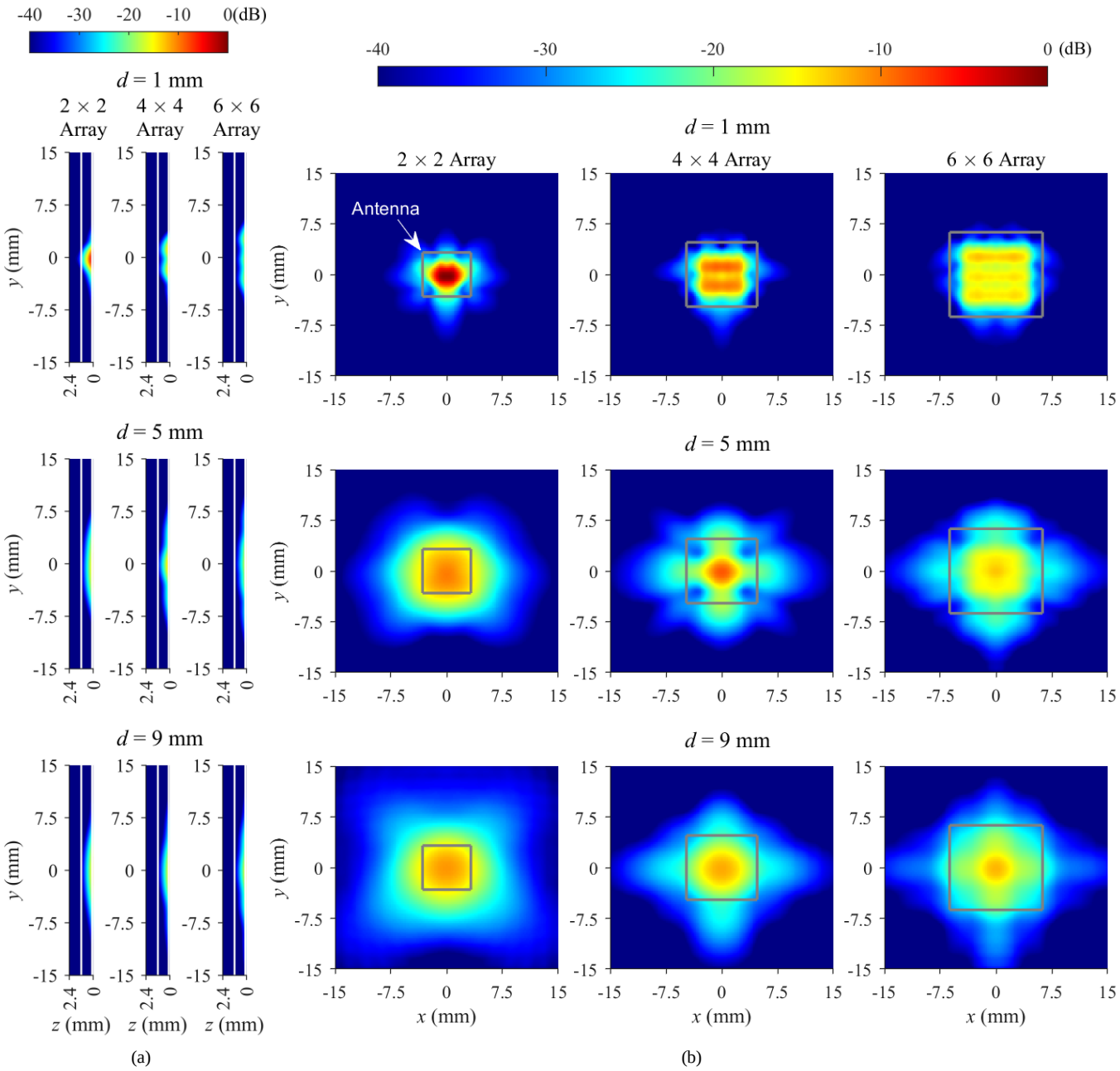

Fig. 10 Distributions for different d (1, 5, 9 mm) and array sizes (2 × 2, 4 × 4, 6 × 6) at 100 GHz. (a) SAR on the *yoz*-plane, which is normalized to the peak SAR value of the 2 × 2 array for d = 1 mm in (a). The white lines are the interface between the different layers of the tissue model. (b) APD on *xoy*-plane for A = 0 cm^2, which is normalized to peak APD value of the 2 × 2 array for d = 1 mm in (b). The gray rectangle in each figure represents antenna models.

REFERENCES

[1] G. Wikström, P. Persson, S. Parkvall, G. Mildh, E. Dahlman, B. Balakrishnan, et al., "6G – Connecting a cyber-physical world," Stockholm, Sweden, Ericsson, White Paper, GFTL-20:001402, Feb. 2022, [Online]. Available: https://www.ericsson.com/4927de/assets/local/reports-papers/white-papers/6g--connecting-a-cyber-physical-world.pdf

[2] ICNIRP, "Guidelines for limiting exposure to electromagnetic fields (100 kHz to 300 GHz)," *Health Phys.*, vol. 118, no. 5, pp. 483–524,2020.

[3] K. Taguchi, S. Kodera, A. Hirata, and T. Kashiwa, "Computation of Absorbed Power Densities in High-Resolution Head Models by Considering Skin Thickness in Quasi-Millimeter and Millimeter Wave Bands," *IEEE J. Elect., RF Micro. Med. Biol.*, Sep. 2022.

[4] K. Li, K. Sasaki, K. Wake, T. Onishi, and S. Watanabe, "Quantitative comparison of power densities related to electromagnetic near-field exposures with safety guidelines from 6 to 100 GHz," *IEEE Access*, vol. 9, pp. 115801–115812, 2021.

[5] N. Miura, S. Kodera, Y. Diao, J. Higashiyama, Y. Suzuki, and A. Hirata, "Power absorption and skin temperature rise from simultaneous near-field exposure at 2 and 28GHz," *IEEE Access*, vol. 9, pp. 152140–152149, Nov. 2021.

[6] Y. Diao and A. Hirata, "Exposure assessment of array antennas at 28 GHz using hybrid spherical near-field transformation and FDTD method," *IEEE Trans. Electromagn. Compat.*, vol. 63, no. 5, pp. 1690–1698, Oct. 2021.

[7] Y. Diao, E. A. Rashed, and A. Hirata, "Assessment of absorbed power

density and temperature rise for nonplanar body model under electromagnetic exposure above 6 GHz," *Phys. Med. Biol.*, vol. 65, no. 22, p. 224001, 2020.

[8] K. Li, K. Sasaki, S. Watanabe, and H. Shirai, "Relationship between power density and surface temperature elevation for human skin exposure to electromagnetic waves with oblique incidence angle from 6 GHz to 1 THz," *Phys. Med. Biol.*, vol. 64, no. 6, p. 065016, 2019.

[9] K. Sasaki, M. Mizuno, K. Wake, and S. Watanabe, "Monte Carlo simulations of skin exposure to electromagnetic field from 10 GHz to 1 THz," *Phys. Med. Biol.*, vol. 62, no. 17, p. 6993, 2017.

[10] D. Funahashi, A. Hirata, S. Kodera, and K. R. Foster, "Area-averaged transmitted power density at skin surface as metric to estimate surface temperature elevation," *IEEE Access*, vol. 6, pp. 77665–77674, 2018.

[11] E. Lemay, G. B. Gajda, G. W. McGarr, M. Zhuk, and J. Paradis, "Analysis of ICNIRP 2020 Basic Restrictions for Localized Radiofrequency Exposure in the Frequency Range Above 6 GHz", *Health Phys.*, vol. 123, no. 3, pp. 179–196, Sep. 2022.

[12] B. Xu, K. Zhao, Z. Ying, D. Sjoberg, W. He, and S. He, "Analysis of Impacts of Expected RF EMF Exposure Restrictions on Peak EIRP of 5G User Equipment at 28 GHz and 39 GHz Bands," *IEEE Access*, vol. 7, pp. 20996–21005, 2019.

[13] W. He, B. Xu, Y. Yao, D. Colombi, Z. Ying, and S. He, "Implications of Incident Power Density Limits on Power and EIRP Levels of 5G Millimeter-Wave User Equipment" *IEEE Access*, vol. 8, pp. 148214-148225, 2020.

[14] W. He, B. Xu, L. Scialacqua, Z. Ying, A. Scannavini, L. J. Foged, et al., "Fast power density assessment of 5G mobile handset using equivalent currents method," *IEEE Trans. Antennas Propag.*, vol. 69, no. 10, pp. 6857–6869, 2021.

[15] H. H. Pennes, "Analysis of tissue and arterial blood temperatures in the resting human forearm," *J. Appl. Physiol*., vol. 1, no. 2, pp. 93–122, 1948.

[16] A. Hirata, S. Kodera, K. Sasaki, J. Gomez-Tames, I. Laakso, A. Wood, S. Watanabe, and K. R. Foster, "Human exposure to radiofrequency energy above 6 GHz: Review of computational dosimetry studies," *Phys. Med. Biol*., vol. 66, no. 8, Apr. 2021, Art. no. 08TR01.

[17] K. Li, Y. Diao, K. Sasaki, A. Prokop, D. Poljak, V. Doric, J. Xi, S. Kodera, A. Hirata, and W. E. Hajj, "Intercomparison of calculated incident power density and temperature rise for exposure from different antennas at 10–90 GHz," *IEEE Access*, vol. 9, pp. 151654–151666, 2021.

[18] Y. Diao, K. Li, K. Sasaki, S. Kodera, I. Laakso, W. E. Hajj, and A. Hirata, "Effect of incidence angle on the spatial-average of incident power density definition to correlate skin temperature rise for millimeter wave exposures," *IEEE Trans. Electromagn. Compat*., vol. 63, no. 5, pp. 1709–1719, 2021

[19] Y. Hashimoto *et al*., "On the averaging area for incident power density for human exposure limits at frequencies over 6 GHz," *Phys. Med. Biol*., vol., 62, no. 8, pp. 3124–3138, 2017.

[20] R. Morimoto, A. Hirata, I. Laakso, M. C. Ziskin, and K. R. Foster, "Time constants for temperature elevation in human models exposed to dipole antennas and beams in the frequency range from 1 to 30 GHz," *Phys.Med. Biol*., vol. 62, no. 5, pp. 1676–1699, 2017.

[21] R. Morimoto, I.Laakso,V.De Santis, and A. Hirata, "Relationship between peak spatial-averaged specific absorption rate and peak temperature elevationin human head in frequency range of 1-30 GHz," *Phys. Med. Biol*., vol. 61, no. 14, pp. 5406–5425, 2016.

[22] W. He, B. Xu, M. Gustafsson, Z. Ying, and S. He, "RF Compliance Study of Temperature Elevation in Human Head Model Around 28 GHz for 5G User Equipment Application: Simulation Analysis," *IEEE Access*, vol. 6, pp. 830-838, 2017.